Available on CMS information server **CMS NOTE 2005/007**

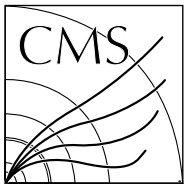

The Compact Muon Solenoid Experiment

CMS Note

Mailing address: CMS CERN, CH-1211 GENEVA 23, Switzerland

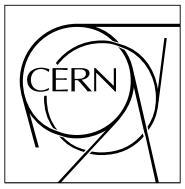

8 April 2005

Search for radion decays into Higgs boson pairs in the $\gamma\gamma b\bar{b}$, $\tau^+\tau^- b\bar{b}$ and $b\bar{b}b\bar{b}$ final states

D. Dominici,

Università di Firenze and I.N.F.N., Italy

G. Dewhirst, A. Nikitenko

Imperial College, London, UK

S. Gennai,

Scuola Normale Superiore and I.N.F.N., Pisa, Italy

L. Fanò,

Università di Perugia and I.N.F.N., Italy

Abstract

The CMS discovery potential for radion decays into two Higgs bosons in the $\gamma\gamma b\bar{b}$, $\tau^+\tau^- b\bar{b}$ and $b\bar{b}b\bar{b}$ final states is studied. The case of a radion mass of 300 GeV/c^2 and a Higgs boson mass of 125 GeV/c^2 is considered. The discovery reach with 30 fb^{-1} in the plane of two parameters of the Randall-Sundrum model, ξ and Λ_ϕ, is evaluated.

1 INTRODUCTION

The Randall Sundrum model (RS) [1, 2] has recently received much attention because it could provide a solution to the hierarchy problem [3], by means of an exponential factor in a five dimensional non-factorizable metric. In the simplest version the RS model is based on a five dimensional universe with two four-dimensional hypersurfaces (branes), located at the boundary of the fifth coordinate y. By placing all the Standard Model fields on the visible brane at $y = 1/2$ all the mass terms, which are of the order of the Planck mass, are rescaled by the exponential factor, to a scale of the order of a TeV. The fluctuations in the metric in the fifth dimension are described in terms of a scalar field, the radion, which in general mixes with the Higgs boson. This scalar sector of the RS model is parametrized in terms of a dimensionless Higgs boson−radion mixing parameter ξ, of the Higgs boson and radion masses $\mathrm{m_h}$, m_ϕ and the vacuum expectation value of the radion field Λ_ϕ.

The phenomenology of Higgs boson and radion at LHC has been subject to several studies [4, 5, 6, 7, 8, 9] concentrating mainly on Higgs and radion processes. The Higgs boson and radion detection is not guaranteed in all the parameter space region. The presence in the Higgs radion sector of trilinear terms opens the possibility of $\phi \to \mathrm{hh}$ and $\mathrm{h} \to \phi\phi$ decays. For example, for $\mathrm{m_h} = 120$ GeV/c^2, $\Lambda_\phi = 5$ TeV and $\mathrm{m}_\phi \sim 250$-350 GeV/c^2 the $\mathrm{BR}(\phi \to \mathrm{hh})$ ranges between 20 and 30 %.

In this note, the CMS discovery potential is estimated for the decay of a radion in a pair of Higgs bosons, in the $\gamma\gamma\mathrm{b\bar{b}}$, $\tau^+\tau^-\mathrm{b\bar{b}}$ and $\mathrm{b\bar{b}b\bar{b}}$ final states and an integrated luminosity of 30 fb^{-1} in the low luminosity run conditions of LHC (peak luminosity of L=2×10^{33}cm^{-2}s^{-1}). The study has been carried out for a radion mass of 300 GeV/c^2 and a Higgs boson mass of 125 GeV/c^2. The sensitivity was evaluated in the (ξ, Λ_ϕ) plane, with systematics uncertainties included.

2 Event Generation

2.1 Signal

Signal events $\mathrm{gg} \to \phi \to \mathrm{hh}$ were generated with PYTHIA [10]. The radion width was set to 0.8 GeV i.e. much smaller than the mass resolution in the detector. The CTEQ5L Parton Density Function (PDF) set was used. The production cross section of the radion in $\mathrm{gg} \to \phi$ process was calculated as

$$\sigma(\mathrm{gg} \to \phi) = \sigma(\mathrm{gg} \to \mathrm{H_{SM}}) \cdot \frac{\Gamma(\phi)}{\Gamma(\mathrm{H_{SM}})} \cdot \frac{\mathrm{Br}(\phi \to \mathrm{gg})}{\mathrm{Br}(\mathrm{H_{SM}} \to \mathrm{gg})}. \quad (1)$$

The total width and branching ratio for the radion of a mass 300 GeV/c^2 are shown in Fig. 1 as a function of the parameter ξ for two values of Λ_ϕ, 1 and 5 TeV. The values of $\sigma(\mathrm{gg} \to \mathrm{H_{SM}})$ (7.52 pb), $\Gamma(\mathrm{H_{SM}})$ (8.5 GeV) and $\mathrm{Br}(\mathrm{H_{SM}} \to \mathrm{gg})$ (5.68·10^{-3}) were calculated at the next-to-leading order with HIGLU and HDECAY programs [11]. Figure 2 shows $\sigma(\mathrm{gg} \to \phi)$ and $\mathrm{Br}(\phi \to \mathrm{hh})$ as a function of the parameter ξ. Branching ratios of the Higgs boson in the Standard Model and in the Randall-Sundrum model are similar, as shown in Figure 3a for $\mathrm{m_h}$ = 125 GeV/c^2. Figure 3b presents cross section times branching ratio for the process $\mathrm{gg} \to \phi \to \mathrm{hh} \to \gamma\gamma\mathrm{b\bar{b}}$ as a function of the parameter ξ. For Λ_ϕ = 1 TeV, the maximal cross section times branching ratio is 71 fb reached for $\xi = -0.35$. The maximal cross section times branching ratio for the $\mathrm{b\bar{b}b\bar{b}}$ final state is 10.3 pb

2.2 Background

2.2.1 Background for $\gamma\gamma\mathrm{b\bar{b}}$ final state

The irreducible di-photon backgrounds were generated with CompHEP [12] for the $\gamma\gamma$jj (j=u,d,s,g) process and with MadGraph [13] for the $\gamma\gamma\mathrm{c\bar{c}}$ and $\gamma\gamma\mathrm{b\bar{b}}$ processes. Renormalization and factorization scales, μ_r and μ_f, were set to μ_0 = $\mathrm{M_Z}$ and the CTEQ5L pdf set was chosen. Hadronization was simulated with PYTHIA. Initial and final state radiation (ISR, FSR) were switched on. The generator level preselections are $\mathrm{p^{\gamma}_{T,max\ (min)}}$ >35 (20) GeV/c, $\mathrm{p^{j}_T}$ >20 GeV/c, $|\eta^{\gamma,\mathrm{j}}|$ <2.5, $\Delta\mathrm{R}_{\gamma\gamma}$ >0.3, $\Delta\mathrm{R}_{\gamma\mathrm{j}}$ >0.3,

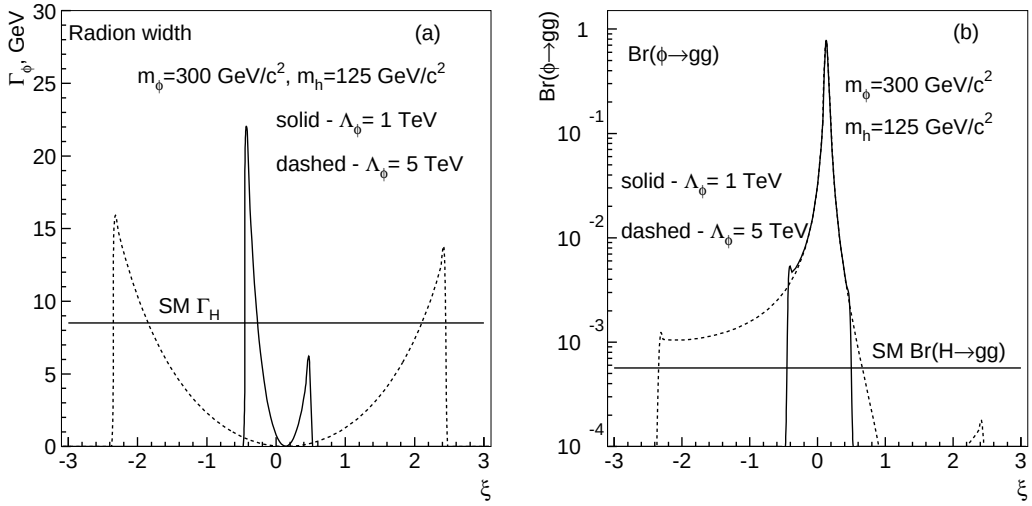

Figure 1: The total width (a) and branching ratio of radion to a pair of gluons (b) for m_{ϕ}= 300 GeV/c^2 as a function of the parameter ξ and for two values of Λ_{ϕ}, 1 and 5 TeV. The values for a SM Higgs boson of 300 GeV/c^2 mass are also shown as horizontal lines.

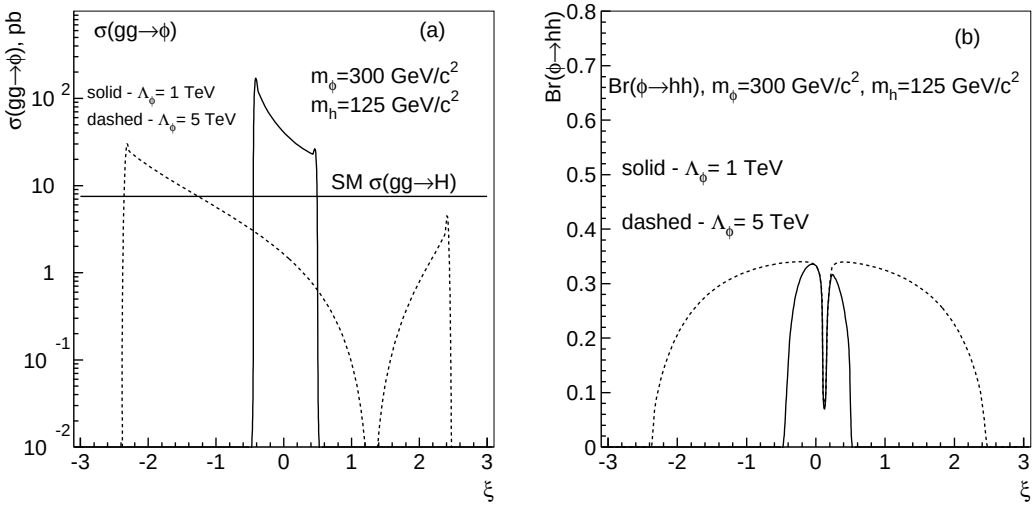

Figure 2: $\sigma(\mathrm{gg} \rightarrow \phi)$ (a) and Br($\phi \rightarrow \mathrm{hh}$) (b) as a function of the parameter ξ for two values of Λ_{ϕ}, 1 and 5 TeV. On the left plot the cross section of $\mathrm{gg} \rightarrow \mathrm{H_{SM}}$ process for the SM Higgs boson of 300 GeV/c^2 mass is also shown as the horizontal line.

$\Delta \mathrm{R_{jj}} > 0.3$, where $\Delta \mathrm{R}$ is the distance in the (η, φ) space. The leading order cross sections obtained with these generators are shown in Table 1 together with the number of events expected with 30 fb^{-1}. The next-to-leading order cross sections are presently unknown [14]. Figure 4 and Figure 5 show jet and photon transverse momentum and pseudorapidity for the $\gamma\gamma$jj background.

The reducible background from γ + three jets and four-jet processes still has to be evaluated. From preliminary inclusive $\mathrm{h} \rightarrow \gamma\gamma$ studies it was assumed that the reducible background is about of 40 % of the total background after all selections [15]. A similar value was obtained in a parton level study [16], in which irreducible and reducible backgrounds to the SM and MSSM double Higgs boson production with $\gamma\gamma\mathrm{b\bar{b}}$ final state were estimated using $\mathrm{jet} \rightarrow \gamma$ misidentification probability and the b-tagging performance from ATLAS.

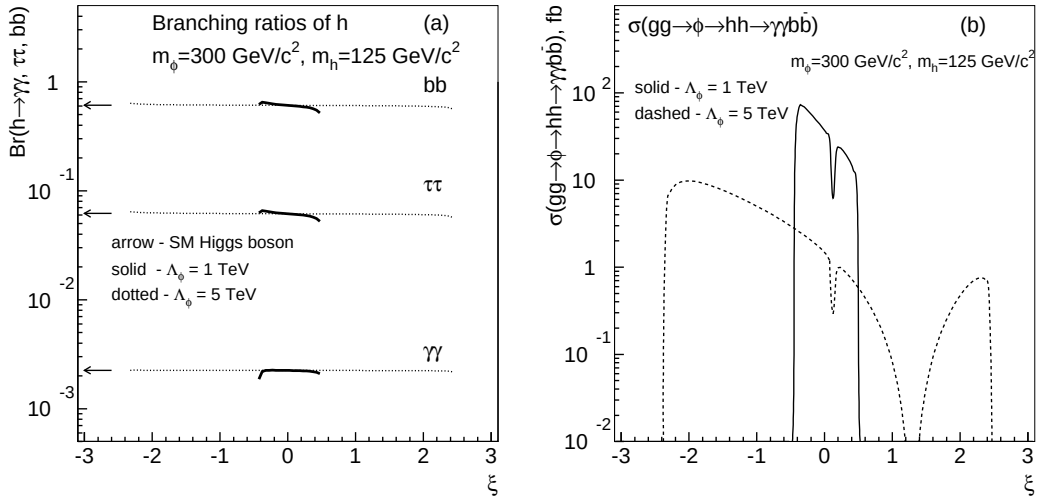

Figure 3: (a): Branching ratios of the Higgs boson in the Standard Model and in the Randall-Sundrum model for m_h = 125 GeV/c^2. (b): cross section times branching ratios for the process $gg \to \phi \to hh \to \gamma\gamma b\bar{b}$ as a function of the parameter ξ for two values of Λ_ϕ, 1 and 5 TeV.

Table 1: Irreducible background cross sections and expected number of events with 30 fb^{-1}.

Process	$\gamma\gamma$jj	$\gamma\gamma c\bar{c}$	$\gamma\gamma b\bar{b}$
Cross section, fb	13310	778	76
Events with 30 fb^{-1}	3.99×10^6	2.33×10^4	2.28×10^3

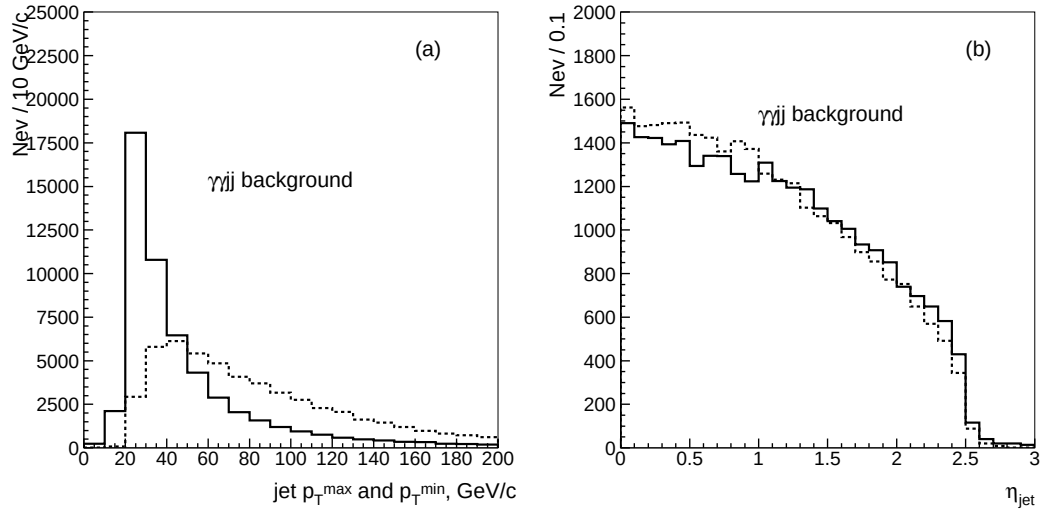

Figure 4: Jet p_T^{max} and p_T^{min} (a) and η of jet with maximal and minimal p_T (b) for the $\gamma\gamma$jj background.

2.2.2 Background for $\tau\tau b\bar{b}$ final state

The signature for the $\tau^+\tau^- b\bar{b}$ final state is an isolated lepton from a leptonic τ decay and three jets (two b jets and one τ jet). The background processes considered are shown in Table 2. They were generated with PYTHIA 6.158 apart from $Zb\bar{b}$ background which was generated with CompHEP. The next-to-leading order (NLO) cross sections, taken from Ref.[17], and the number of events expected with 30 fb^{-1} are also shown in Table 2. The Z+jets (W+jets) samples were generated with $\hat{p}_T > 20$ (80) GeV/c.

Table 3 shows the k factors (ratios of NLO to LO cross sections) as well as theoretical uncertainties taken from Ref.[17].

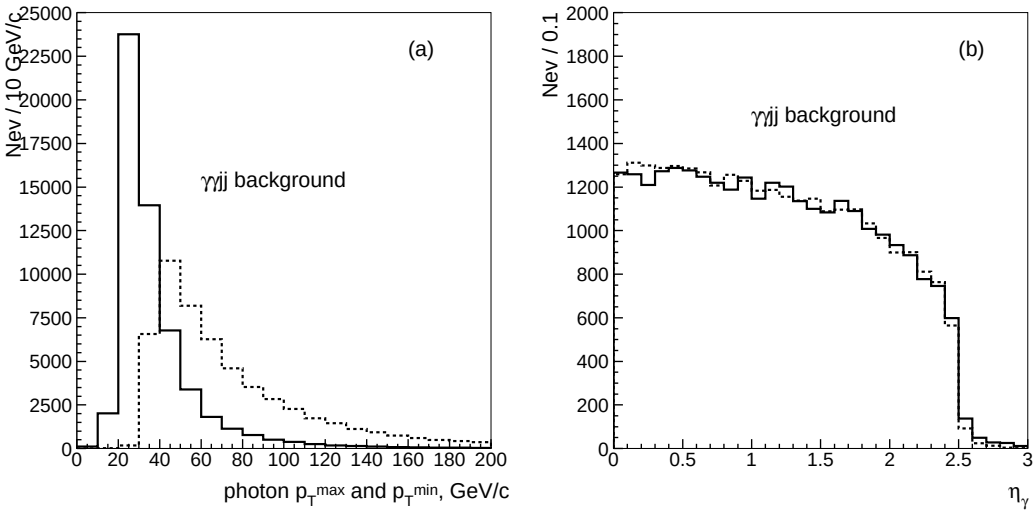

Figure 5: Parton kinematics for $\gamma\gamma$jj background. Photon $\mathrm{p_T^{max}}$ and $\mathrm{p_T^{min}}$ (a); η of photon with maximal and minimal $\mathrm{p_T}$ (b).

Table 2: The next-to-leading order cross section times branching ratio and the numbers of events expected with 30 fb^{-1} for the backgrounds.

Background process	σ (pb)	$\sigma \times$ BR (pb)	Events with 30 fb^{-1}
$\mathrm{t\bar{t}} \to \mathrm{Wb} + \mathrm{W\bar{b}} \to \ell + \nu + \mathrm{jets} + \mathrm{b\bar{b}}$ ($\mathrm{tt_{had}}$)	825	245	7.3×10^6
$\mathrm{t\bar{t}} \to \mathrm{Wb} + \mathrm{W\bar{b}} \to \ell + \nu + \tau$ jet $+ \mathrm{b\bar{b}}$ ($\mathrm{tt_{tau}}$)	825	27	8×10^5
$\mathrm{Zb\bar{b}} \to \tau\tau + \mathrm{b\bar{b}}$	525	8	2.4×10^5
$\mathrm{Z} + \mathrm{jets} \to \tau\tau + \mathrm{jets}$ ($\hat{\mathrm{p}}_\mathrm{T} > 20$ GeV/c)	23300	355	10.6×10^6
$\mathrm{W} + \mathrm{jets} \to \ell + \nu + \mathrm{jets}$ ($\hat{\mathrm{p}}_\mathrm{T} > 80$ GeV/c)	4100	900	27×10^6

Table 3: The k factors (ratios of NLO and LO cross sections) for the backgrounds and theoretical uncertainties [17].

Process	k factor	$\mathrm{k_{min}}$	$\mathrm{k_{max}}$
$\mathrm{t\bar{t}}$	1.35	1.28	1.45
$\mathrm{Zb\bar{b}}$	1.49	1.3	1.7
Z + jets	1.16	1.13	1.19
W + jets	1.13	1.10	1.17

The $\mathrm{t\bar{t}}$ background when both W bosons decay into τ's ($\mathrm{tt_{2tau}}$ sample) was not simulated , but its contribution to the total number of background events was estimated. The cross section times branching ratios for such a process is around 9 pb, about of 30 % of the $\mathrm{tt_{tau}}$ sample (the background process shown in the second row of Table 2).

2.2.3 Backgroung for $\mathrm{b\bar{b}b\bar{b}}$ final state

The backgrounds considered in the analysis of the four b-jet final state are QCD multi-jet production, $\mathrm{t\bar{t}}$ and $\mathrm{Zb\bar{b}}$ (generated with CompHEP). The main contribution comes from QCD with $\hat{\mathrm{p}}_\mathrm{T} > 100$ GeV/c. The dominant background is expected with four bottom quarks in the final state coming from initial and final state radiation and gluon splitting in QCD multi-jet production. Details can be found in Section 6.4.

Table 4 summarizes the signal and background cross sections, the numbers of events expected with 30

fb^{-1} and the number of the events generated.

Table 4: Background cross sections and numbers of events expected with 30 fb^{-1}; the last column shows the numbers of events simulated.

	σ	N events with 30 fb^{-1}	N simulated events
QCD $\hat{p}_T$ (30-50) GeV/c	0.1957 mb	5.9×10^{12}	2.6×10^7
QCD $\hat{p}_T$ (50-80) GeV/c	0.0258 mb	7.7×10^{11}	4×10^6
QCD $\hat{p}_T$ (80-120) GeV/c	0.0036 mb	1.0×10^{11}	3×10^6
QCD $\hat{p}_T$ (120-170) GeV/c	0.0006 mb	1.8×10^{10}	6×10^5
$t\bar{t}$	615 pb	1.8×10^7	5×10^3
$Zb\bar{b}$	349 pb	1.0×10^7	5×10^3

3 Event simulation and reconstruction

The full detector simulation and reconstruction was performed for the signal in the $\gamma\gamma b\bar{b}$ and $\tau^+\tau^- b\bar{b}$ modes. All backgrounds were processed with the CMSJET package [18], which provides a fast simulation of the detector and physics object reconstruction. The signal in the $b\bar{b}b\bar{b}$ was processed with both fast and full simulations. The pile-up conditions corresponding to a luminosity $2\times10^{33}cm^{-2}s^{-1}$ was taken into account in the simulations.

Jets were reconstructed with a cone-based algorithm with a cone size 0.5. Tagging of b jets was performed with the impact parameter method [19]: at least two tracks per jet must have a transverse impact parameter significance larger than 2. For the background events, for which the fast simulation was used, an average b-tagging efficiency of 0.5 was applied for the b jets, 0.1 for the c jets and 0.01 for u, d and s jets and gluons. These numbers correspond to what is obtained on average with the full detector simulation [19] with the impact parameter tagging method. The details on the photon, track and τ-jet reconstruction are given in the following sections.

4 Selection of the $\gamma\gamma b\bar{b}$ final state

At the scale Λ_ϕ = 1 TeV the maximal signal cross section times branching ratio for $\gamma\gamma b\bar{b}$ final state is 83 fb, thus 2490 signal events are expected to be produced with an integrated luminosity of 30 fb^{-1}. The p_T and η distributions of the photons at the PYTHIA generator level, are shown in Figures 6a and b. The two high p_T photons in the final state allow the effective use of the di-photon trigger optimized for the inclusive $h \to \gamma\gamma$ search [21].

4.1 Level-1 and High-Level Trigger selections

Events were required to pass the standard CMS Level-1 and Level-2 double e/γ trigger and to be rejected by the Level-2.5 pixel matching criteria. Di-photon thresholds of 40 and 25 GeV were applied on the transverse energies of the Level-2 e/γ candidates [21].

4.2 Vertex reconstruction and $h \to \gamma\gamma$ mass reconstruction

An event-by-event signal vertex is reconstructed from the track segments found in the Pixel detector as described in [21]. These tracks are referred as "pixel lines" in the following. The vertex with the maximal sum p_T of the pixel lines was chosen as a signal vertex. In Figure 7a is displayed the difference in the z coordinate (along the beam axis) between the true signal vertex and the vertex reconstructed as explained above. In 97 % of the events, the candidate primary vertex is found within a $\pm$ 200 μm window around the true position of the signal vertex. The presence of two calorimeter jets with $E_T > 30$ GeV and $|\eta| < 2.4$ was required before the vertex reconstruction. For the di-photon invariant mass reconstruction

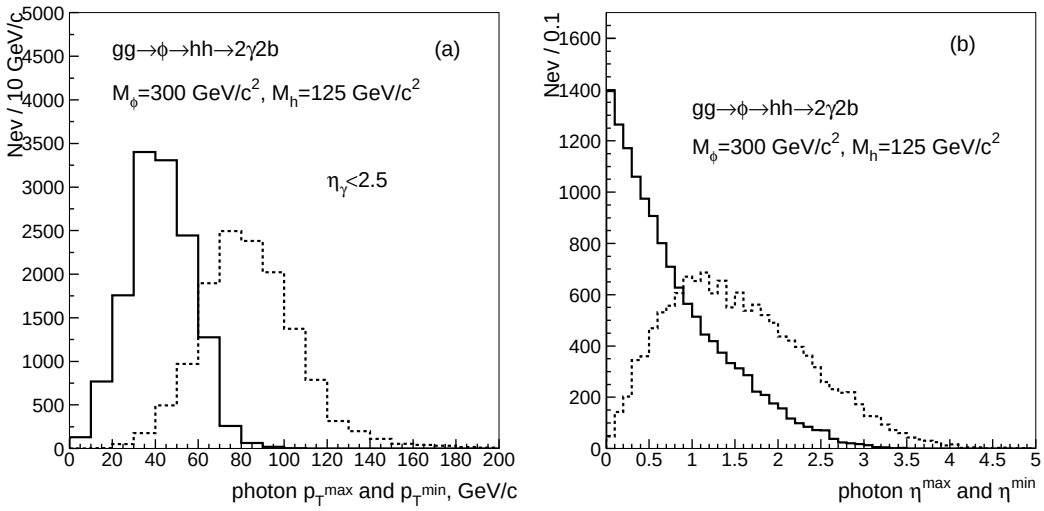

Figure 6: Photon kinematics from PYTHIA simulation. (a): photon $\mathrm{p_T^{max}}$ and $\mathrm{p_T^{min}}$; (b): photon $\eta^{\max}$ and $\eta^{\min}$.

the energies and the directions (corrected for the vertex position) of the two highest $\mathrm{E_T}$ Level-2 e/γ candidates are used. In Figure 7b is shown the reconstructed di-photon invariant mass without and with the vertex position correction. In the event selection the di-photon mass, $\mathrm{M_{\gamma\gamma}}$, was required to be in a window of $\mathrm{m_h}\pm$ 2 GeV/c^2.

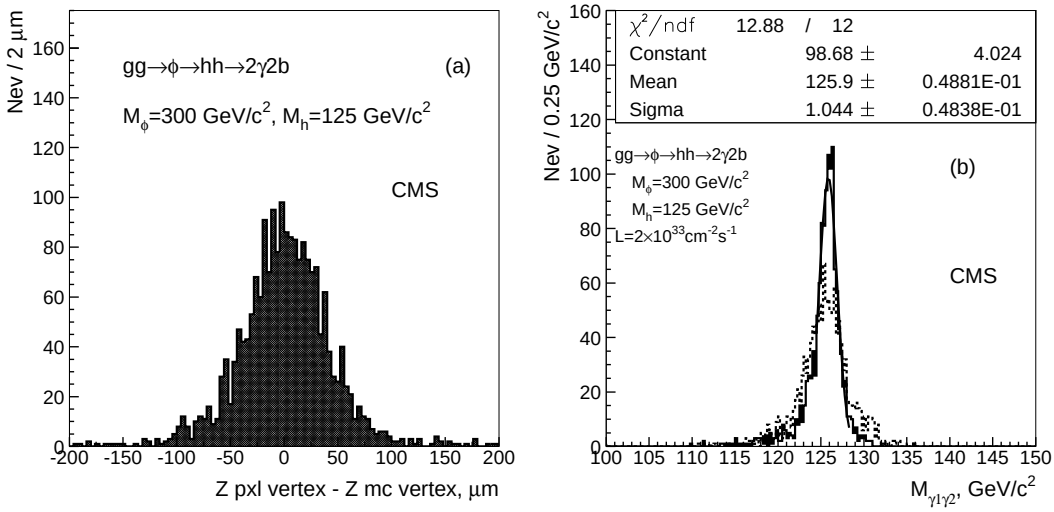

Figure 7: (a): the difference in z coordinate between the simulated signal vertex and the reconstructed vertex; (b): the reconstructed di-photon invariant mass without (dashed) and with (solid) the vertex position corrections.

4.3 Tracker and calorimeter isolation for photons.

The tracks are reconstructed with the Combinatorial Track Finder [21] using the pixel lines from the signal vertex as seeds. The minimal number of reconstructed hits per track is set to 5. Tracks with $\mathrm{p_T} > 1.5$ GeV/c are counted in the cone 0.3 around the photon candidates. The event is accepted if no tracks are found for both photon candidates. The cuts on the track $\mathrm{p_T}$ and the size of the isolation cone are taken following the preliminary results on the tracker isolation for the photons from the inclusive $\mathrm{h} \to \gamma\gamma$ channel presented in Ref.[22]. The distributions of the number of reconstructed tracks ($\mathrm{p_T} >$

1.5 GeV/c) from the signal vertex and within a cone of 0.3 around the first and second photon directions (photons are ordered in $\mathrm{E_T}$) are shown in the left plot of Figure 8a. The difference in the distributions for the first and the second photon is due to that the first photon is more separated from the b jets than the second one, therefore it is more isolated. The distance $\Delta\mathrm{R}_{\gamma\mathrm{b}}$ between the photons and the b-quarks at generator level is shown in Figure 8b. The difference is visible and leads to different isolation efficiencies for the first and the second photon.

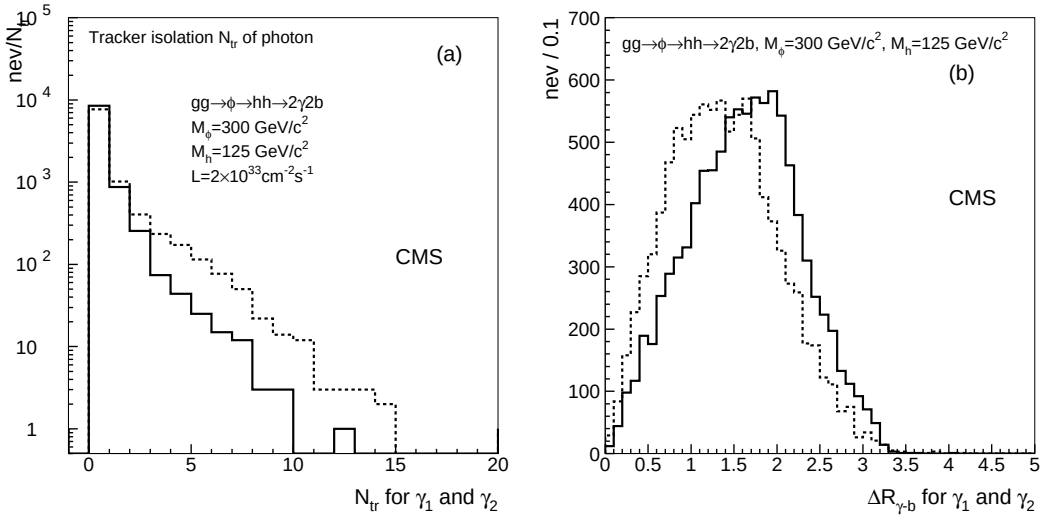

Figure 8: Number of reconstructed tracks with $\mathrm{p_T} > 1.5$ GeV/c from the signal vertex and within a cone $\Delta\mathrm{R}$ = 0.3 around the first and the second photon ordered in $\mathrm{E_T}$ (a); The distance $\Delta\mathrm{R}_{\gamma\mathrm{b}}$ between the photons and the b quarks (b). The solid (dashed) line corresponds to the first (second) photon.

Isolation with clusters in the electromagnetic calorimeter is also applied. The isolation parameter $\mathrm{P_{isol}}$ is defined as the difference between the sum of the transverse energy of the crystals in the cone 0.3 around the photon candidate and the sum of the transverse energies of the clusters forming the Level-2 e/γ super cluster. The size of the isolation cone of 0.3 was used following the preliminary study of the ECAL isolation presented in [23]. The cut on the isolation parameter is set to 5.3 GeV for each photon. Figure 9 shows the isolation parameter $\mathrm{P_{isol}}$ for the first and the second photon. Negative values of $\mathrm{P_{isol}}$ are due to the noise fluctuation in the isolation cone when no-zero-suppressed crystal energies are taken in the selective readout scheme.

4.4 Selection of jets, $\mathrm{h} \to \mathrm{b\bar{b}}$ and radion mass reconstruction

Events with only two calorimeter jets of $\mathrm{E_T} > 30$ GeV and within $|\eta| < 2.4$ are selected. At least one of these jets must be tagged as a b jet. The requirement of the double b tagging does not improve the discovery potential for this channel. The efficiency of the single b tagging is 0.61 per event. The jets were required to be separated from the photons with $\Delta\mathrm{R}_{\gamma\mathrm{j}} > 0.5$. These two jets were considered as the b-jet candidates from $\mathrm{h} \to \mathrm{b\bar{b}}$. The di-jet mass, $\mathrm{M_{bj}}$, is further required to be in a window $\mathrm{m_h} \pm 30$ GeV/c^2. Finally, the $\mathrm{M_{\gamma\gamma bj}}$ mass must be in a window $\mathrm{m}_\phi \pm 50$ GeV/c^2. The evaluation of the $\mathrm{m_h}$ and m_ϕ values from the data is discussed in the Section 4.6. Figure 10 shows the $\mathrm{M_{bj}}$ and $\mathrm{M_{\gamma\gamma bj}}$ distributions with arbitrary normalization. The dashed histogram in Figure 10a was produced for the events with the correct jet-b quark association for both b quarks. The jet was considered to be associated with the b quark if $\Delta\mathrm{R_{jb}} < 0.5$.

4.5 The signal and background selection efficiencies

Table 5 shows the trigger and off-line selection efficiencies for the signal. The signal efficiency of the

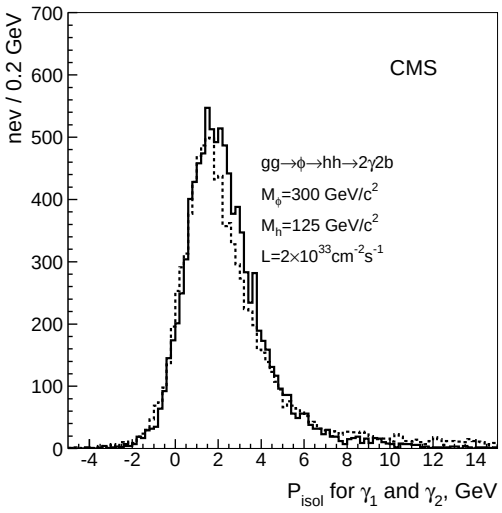

Figure 9: Isolation parameter $\mathrm{P_{isol}}$ for the first and the second photon.

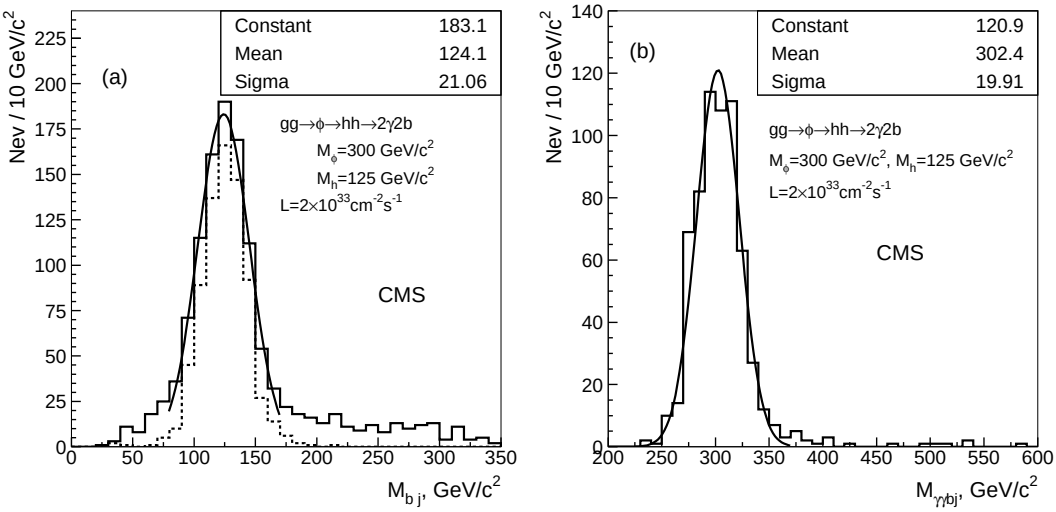

Figure 10: Distributions of the reconstructed bj (a) and $\gamma\gamma$bj (b) masses for the signal. The dashed histogram in Figure 10a is for the events with the correct jet-b quark association for both b quarks.

whole selection chain is 3.7 %.

The efficiencies of the background event selections and the number of events after all cuts expected with 30 fb^{-1} are shown in Table 6. The uncertainty on the number of events expected due to the limited simulated statistics are also shown. The number of the background events has to be still multiplied by 0.92 and by 0.90 to take into account of the Level-1 e/γ trigger and the isolation efficiencies, not taken into account in the fast simulation. These efficiencies were obtained from a full simulation of the signal events. Thus the expected irreducible background is 6.9 events with 30 fb^{-1} after all selections. Figures 11a,b and 12a show, the di-jet, $\mathrm{M_{bj}}$, di-photon, $\mathrm{M_{\gamma\gamma}}$ and $\mathrm{M_{\gamma\gamma bj}}$ mass distributions for the signal and background after all selections except the mass window cuts with 30 fb^{-1}. The signal is shown for the maximal cross section times branching ratio point in the (ξ, Λ_ϕ) plane. Figure 12b shows the $\mathrm{M_{\gamma\gamma bj}}$ mass distribution for the background and signal plus background after all selections with 30 fb^{-1} and for the maximal signal cross section times branching ratio.

Table 5: Trigger and off-line selection efficiencies for the $\gamma\gamma b\bar{b}$ signal.

selection criteria	relative efficiency	absolute efficiency
1. Level-1	0.738	0.738
2. Level-2	0.927	0.685
3. Level-2.5 photon stream	0.996	0.683
4. $E_T^{\gamma 1,2} > 40$, 25 GeV	0.871	0.595
5. tracker isolation of photons	0.682	0.406
6. ECAL isolation of photons	0.909	0.369
7. two jets of $E_T > 30$ GeV, $\|\eta\| < 2.4$	0.341	0.126
8. at least one b jet	0.610	0.077
9. $M_{\gamma\gamma}$ mass window of 4 GeV/c^2	0.779	0.060
10. M_{bj} window 60 GeV/c^2	0.649	0.039
11. $M_{\gamma\gamma bj}$ window 100 GeV/c^2	0.950	0.037

Table 6: Efficiencies and the number of events with 30 fb^{-1} after all selections for the background processes.

	$\gamma\gamma jj$	$\gamma\gamma c\bar{c}$	$\gamma\gamma bb$
selections	efficiency		
1. $E_T^{\gamma 1,2} > 40$, 25 GeV, $\|\eta\| < 2.5$	0.446	0.466	0.487
2. tracker isolation in cone 0.3	0.328	0.345	0.379
3. two jets $E_T > 30$ GeV, $\|\eta\| <2.4$	0.127	0.125	0.133
4. at least one b jet	2.97×10^{-3}	1.76×10^{-2}	9.49×10^{-2}
5. $M_{\gamma\gamma}$ window 4 GeV/c^2	6.50×10^{-5}	3.68×10^{-4}	2.92×10^{-3}
6. M_{bj} window 60 GeV/c^2	2.01×10^{-5}	1.34×10^{-4}	1.02×10^{-3}
7. $M_{\gamma\gamma bj}$ window 100 GeV/c^2	1.05×10^{-5}	8.57×10^{-5}	8.77×10^{-4}
N events after all selections	4.2 ± 0.8	2.0 ± 0.6	2.0 ± 0.6

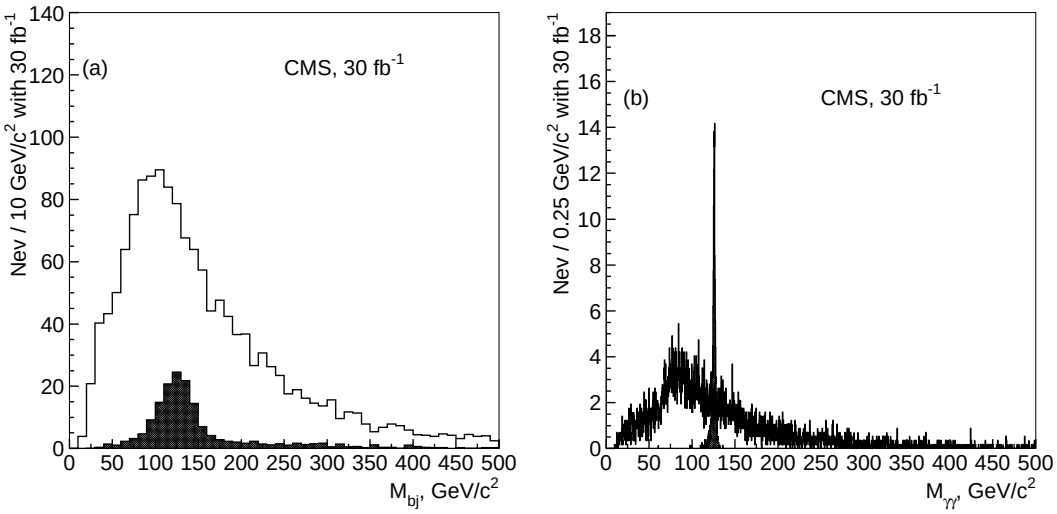

Figure 11: Background (open histogram) and signal (solid histogram) Higgs boson mass candidate distributions after all selections except the mass window cuts with 30 fb^{-1}. Di-jet mass (a) and di-photon mass (b). Signal is shown for the maximal cross section times branching ratios point in (ξ, Λ_ϕ) plane.

4.6 Discovery reach and systematics

4.6.1 Discovery strategy

The discovery strategy for the $\phi \to hh \to \gamma\gamma b\bar{b}$ channel is the following. First, the observation of the peak in the di-photon mass distribution of $\gamma\gamma bj$ events (Figure 11b) indicates the presence of one of

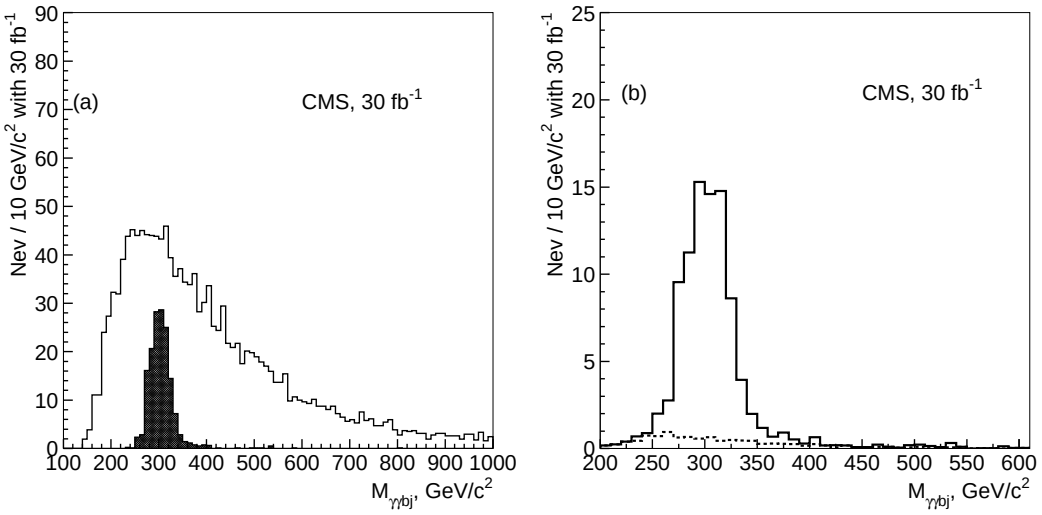

Figure 12: (a) : $M_{\gamma\gamma jj}$ for the signal (solid histogram) and background (open histogram) after all selections except the mass window cuts with 30 fb^{-1}. (b) : $M_{\gamma\gamma bj}$ for the background (dashed histogram) and the signal plus background (solid histogram) after all selections with 30 fb^{-1}. In both plots signal was evaluated for the maximal cross section times branching ratio point in (ξ, Λ_ϕ) plane.

the two Higgs bosons from the radion decay. The events is then counted with the di-photon mass,$M_{\gamma\gamma}$, inside a 4 GeV/c^2 mass window and a di-jet mass, M_{bj}, within a 60 GeV/c^2 mass window centred at the value of the observed $\gamma\gamma$ peak. The radion is found as an excess of events in these two mass windows compared to the background expected (in Figure 12b).

If the di-photon mass peak is not visible due to the small signal cross section, a sliding mass window procedure can be used. The two mass windows are moved in parallel. After the scan, the window position with the largest excess of events compared with the expected background is taken. More precisely, the position is taken where the probability of the background-only hypothesis reaches a minimum. When the signal significance in the selected $M_{\gamma\gamma} - M_{bj}$ window exceeds 5σ, a selection can be done on $M_{\gamma\gamma bj}$, since the signal-over-background ratio (S/B) is larger than unity and the $M_{\gamma\gamma bj}$ distribution of the background is different from that of the signal.

4.6.2 Theoretical uncertainty and discovery reach with the irreducible background

Figure 13a shows the 5σ discovery contour in the the (ξ, Λ_ϕ) plane. The statistical significance was calculated with the Poisson probability. Theoretically excluded regions are also shown in the plot. The dashed line contours present the discovery reach when the irreducible background cross sections are calculated for the renormalization and factorization scales set to $\mu_r = \mu_f = 0.5\times\mu_0$ and to $2\times\mu_0$ ($\mu_0 = M_Z$). Calculations with different scales are done for the $\gamma\gamma b\bar{b}$ background only. It was suggested in [25] that a similar uncertainty can hold the $\gamma\gamma c\bar{c}$ and $\gamma\gamma jj$ backgrounds. A variation of the background cross section of 40 % was found due to a variation of the renormalization and factorization scales from $0.5\times\mu_0$ to $2\times\mu_0$. Figure 13b shows the $M_{\gamma\gamma bj}$ distribution for the background and signal plus background after all selections with 30 fb^{-1}. The signal-plus-background distribution is shown for the (ξ, Λ_ϕ) point (0.4, 1 TeV) where a statistical significance of 5σ is obtained. The dashed histograms corresponds to the irreducible background calculated with the renormalization and factorization scales set to $\mu_r = \mu_f = 0.5\times\mu_0$ and to $2\times\mu_0$.

4.6.3 Discovery reach with the reducible and irreducible backgrounds

Figure 14a shows the 5σ discovery contour in the (ξ, Λ_ϕ) plane when 40 % of the reducible background is added. As in Figure 13 the dashed line contours present the discovery regions when the irreducible

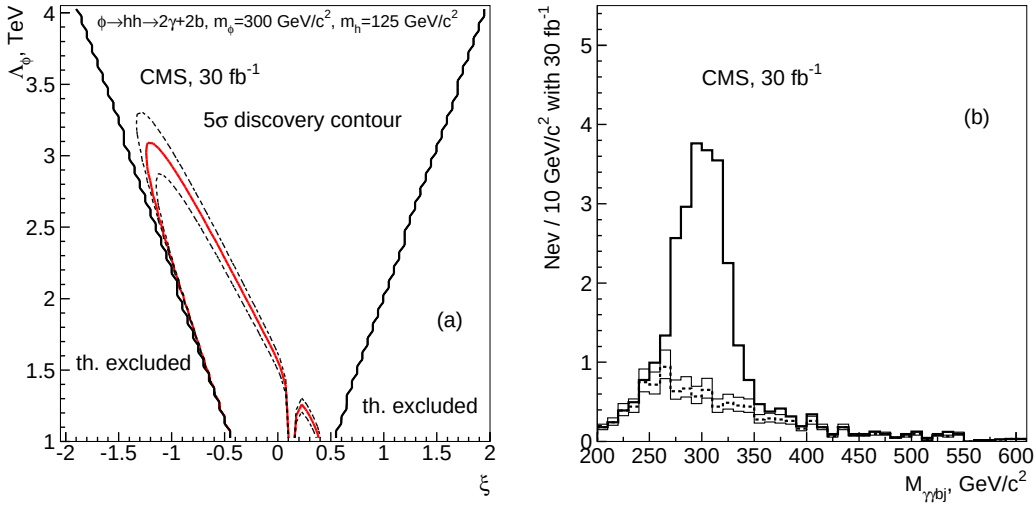

Figure 13: (a): the 5σ discovery contour for the $\phi \to \mathrm{hh} \to \gamma\gamma$+$\mathrm{b\bar{b}}$ channel (m_ϕ=300 GeV/c^2, $\mathrm{m_h}$=125 GeV/c^2) with 30 fb^{-1}; only irreducible backgrounds were taken into account. The dashed line contours present the discovery regions when the irreducible background cross sections were calculated for the renormalization and factorization scales set to $0.5\times\mu_0$ and to $2\times\mu_0$. (b) : the $\mathrm{M}_{\gamma\gamma\mathrm{bj}}$ distribution for the background (thick dashed line) and signal plus background (thick solid line) after all selections with 30 fb^{-1}. Signal-plus-background distribution is shown for the (ξ, Λ_ϕ) point (0.4, 1 TeV) where a statistical significance of 5σ is obtained. The thin solid histograms correspond to the irreducible background calculated with renormalization and factorization scales set to $0.5\times\mu_0$ and to $2\times\mu_0$.

background cross sections are calculated with renormalization and factorization scales set to $0.5\times\mu_0$ and $2\times\mu_0$.

4.6.4 Evaluation of the background from the data and effect of systematic uncertainty

The background can be determined directly from the $\gamma\gamma$-plus-two-jets data obtained after all selections, including b tagging, except the final mass window cuts on $\mathrm{M}_{\gamma\gamma}$, $\mathrm{M_{bj}}$ and $\mathrm{M}_{\gamma\gamma\mathrm{bj}}$. The signal-to-background ratio is always less than 10 % before the mass cuts are applied. The final cuts on $\mathrm{M}_{\gamma\gamma}$, $\mathrm{M_{bj}}$ and $\mathrm{M}_{\gamma\gamma\mathrm{bj}}$ introduce a systematic uncertainty on the number of the background events expected after these cuts. This uncertainty is determined by the following factors : the energy scale uncertainty for the photons and jets, the theoretical uncertainty due to the possible different shape of the mass distributions for the different renormalization, the factorization scales and the different structure functions. The assumption of 0.1 % uncertaincy on the photon scale [20] and 1 % uncertainty of the jet scale [21] leads to 1.4 % incertainty on $\mathrm{M}_{\gamma\gamma}$ cut efficiency and 1 % uncertainty of $\mathrm{M_{bj}}$ cut efficiency. The variation of the renormalization and factorization scale leads to $\simeq$ 3 % uncertainty in the efficiency of the mass cuts. This value is expected to be smaller with the next-to-leading order calculations, still missing in the literature. The right plot in Figure 14b shows two contours with and without the systematic uncertainty discussed above. The contours are evaluated with the total background and for the irreducible background cross sections calculated with the scale $\mu = \mu_0$.

4.6.5 Radion and Higgs boson search complementarity

Figure 15 shows the regions in (M_ϕ, ξ) parameter space where the significance of the Higgs boson discovery combining $\mathrm{h} \to \gamma\gamma$, $\mathrm{t\bar{t}h}$ ($\mathrm{h} \to \mathrm{b\bar{b}}$), $\mathrm{h} \to \mathrm{ZZ}^* \to 4\ell$, $\mathrm{h} \to \mathrm{WW}^* \to 2\ell$, qqh ($\mathrm{h} \to \tau\tau$) and Wh ($\mathrm{h} \to \gamma\gamma$) channels drops below 5σ level and the regions where the significance of the radion discovery with the $\phi \to \mathrm{ZZ}^{(*)} \to 4\ell$ mode exceeds 5σ with 30 fb^{-1}. These contours are obtained for the value of $\mathrm{m_h}$ = 125 GeV/c^2 used in this study and for two values of the scale Λ_ϕ, 1 TeV/c^2 (a) and 2 TeVc^2

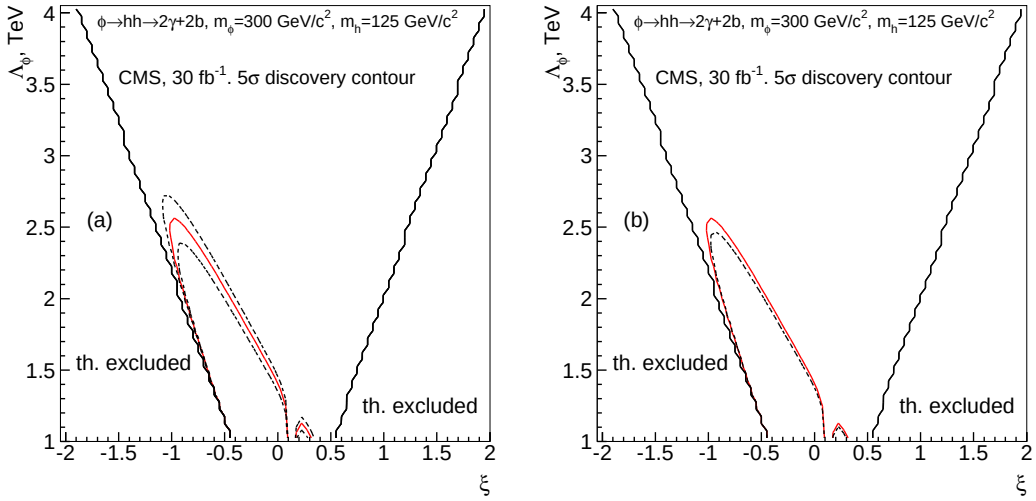

Figure 14: The 5σ discovery contours for $\phi \to \mathrm{hh} \to \gamma\gamma$+$\mathrm{b\bar{b}}$ channel (m_ϕ=300 GeV/c^2, $\mathrm{m_h}$=125 GeV/c^2) with 30 fb^{-1}. In (a) the solid contour shows the discovery region for the renormalization and factorization scales $\mu_\mathrm{r} = \mu_\mathrm{f} = \mathrm{M_Z}$. The dashed contours refer to $\mu_\mathrm{r} = \mu_\mathrm{f} = 0.5\ \mathrm{M_Z}$ and $2\ \mathrm{M_Z}$. In (b) the solid (dashed) contours show the discovery region without (with) the effects of the systematic uncertainties for $\mu_\mathrm{r} = \mu_\mathrm{f} = \mathrm{M_Z}$.

(b). The Higgs boson observability was evaluated using the results published in Ref [26]. The outermost contours define the theoretically allowed region. The light grey regions show the part of the parameter space where the significance of the Higgs boson discovery drops below 5σ level. The regions inside the thick curves are the ones where the significance of the $\phi \to \mathrm{ZZ}^{(*)} \to 4\ell$ signal exceeds 5σ. A comparison of Figure 15 with the discovery contours for $\phi \to \mathrm{hh} \to \gamma\gamma\mathrm{b\bar{b}}$ channel shown in Figure 14 shows that in the region of negative ξ, where the Higgs boson cannot be discovered, the $\phi \to \mathrm{hh} \to \gamma\gamma\mathrm{b\bar{b}}$ and $\phi \to \mathrm{ZZ}^{(*)} \to 4\ell$ channels can be found. Thus, the observation of both the $\phi \to \mathrm{hh} \to \gamma\gamma\mathrm{b\bar{b}}$ and $\phi \to \mathrm{ZZ} \to 4\ell$ channels and the cross section measurement could with 30 fb^{-1} identify the existence of the radion in the region $\mathrm{M}_\phi > 2\mathrm{M_h}$. In certain ($\mathrm{M}_\phi$, ξ) regions, the observation of a clear peak in the di-photon mass distribution of $\gamma\gamma\mathrm{bj}$ events would be possible, thus giving the possibility to measure the Higgs boson mass, even if the Higgs boson is not observed in the channels listed above. In the study of $\tau\tau\mathrm{b\bar{b}}$ and $\mathrm{b\bar{b}b\bar{b}}$ final states presented below this possibility is exploited.

5 Analysis of the $\tau^+\tau^-\mathrm{b\bar{b}}$ final state

The signature for which one τ decays leptonically and the other τ decays hadronically (producing a τ jet) is considered in this session. For the signal, the largest cross section times branching ratios is 0.96 pb at $\xi = -0.35$ and Λ_ϕ=1 TeV. About 29 000 signal events are expected to be produced at maximum with an integrated luminosity of 30 fb^{-1}.

5.1 Trigger selection

The lepton and the τ jet from the signal are not energetic enough to pass efficiently the Level-1 single electron or single τ-jet trigger thresholds [21]. The combined electron-plus-τ-jet trigger has more suitable thresholds as shown in Table 7. The single muon trigger threshold is loose enough to provide a good efficiency. To increase the background rejection, however, the combined Level-1 muon-plus-τ-jet trigger with $\mathrm{p_T^{\mu}} > 14$ GeV/c and $\mathrm{E_T^{\tau\ jet}} > 35$ GeV is required.

The High–Level muon or electron trigger is applied to the events passing the combined Level-1 electron(muon)-plus-τ jet trigger. Events passing these two trigger steps are then required to satisfy the High–Level τ trigger [21]. The standard High–Level τ trigger would be applied to the most energetic

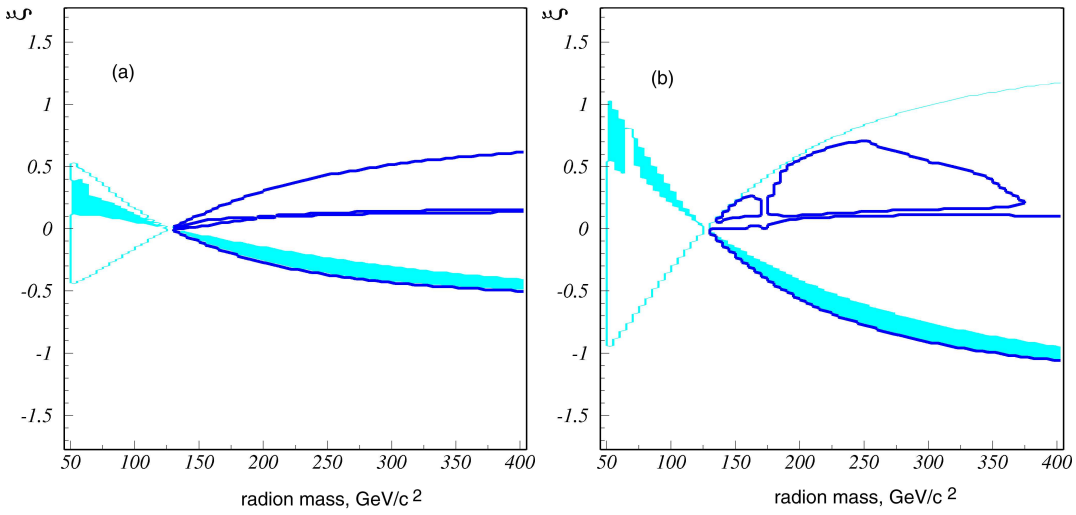

Figure 15: The light grey (cyan) regions show the part of the (M_ϕ, ξ) parameter space where the significance of the Higgs boson discovery with $h \to \gamma\gamma$, $t\bar{t}h$ ($h \to b\bar{b}$), $h \to ZZ^* \to 4\ell$, $h \to WW^* \to 2\ell$, qqh ($h \to \tau\tau$) and Wh ($h \to \gamma\gamma$) channels drops below 5σ. The regions inside thick (blue) curves are the ones where the significance of the $\phi \to ZZ^{(*)} \to 4\ell$ signal exceeds 5σ. The outermost contours define the theoretically allowed region. Results are presentd for m_h=125 GeV/c^2, Λ_ϕ = 1 TeV (a) and 2 TeV (b) and for 30 fb^{-1}.

Table 7: Level-1 Trigger table at low luminosity. The thresholds correspond to 95% efficiency, taken from [21].

Trigger	Threshold (GeV)
Inclusive isolated electron/photon	29
Inclusive isolated muon	14
Single tau-jet trigger	86
Electron&&Jet	21*45

τ jet in the τ-jet list provided by Level-1 trigger. However, the low purity of the Level-1 τ-jet trigger for the τ jets with $E_T < 50$ GeV depends on the event topology [21]. In order to increase the signal efficiency, the High–Level τ-trigger algorithm is applied to the three highest–E_T jets reconstructed at HLT. The following parameters were used for the HLT algorithm: a matching cone ΔR = 0.1, an isolation cone ΔR = 0.4, a signal cone ΔR = 0.07, P_T of the most energetic track greater than 10 GeV and only events with one or three reconstructed charged particle tracks in the signal cone were accepted. The identified electron may also be found in the jet list, misidentified as a calorimetric jet. It is therefore required that the distance in the (η-φ) plane between the electron and the τ jet ($\Delta R_{\ell\tau}$) be greater than 0.1.
The value of the τ-tagging efficiency and mistagging rate used to parametrize the fast simulation package were determined using fully simulated samples of QCD and single τ events. The Level-1 τ mistagging efficiency varies from 66% to 85% (depending on the jet energy); the efficiency of the High–Level trigger lepton isolation is around 35% for electrons and 50% for muons. These efficiencies have been implemented in the fast simulation to estimate the global Trigger response. The Trigger selection efficiency is shown in Table 8 for the signal and background samples.

5.2 Off-line analysis

Events selected at HLT are further reconstructed off-line to separate signal events from background events. First, the neutrino momenta are inferred from the transverse missing energy and the Higgs boson

Table 8: Trigger efficiency for signal and background samples. The L1 columns refer to the Level-1 trigger efficiency, and the HLT columns to the High Level trigger efficiency. The last column is the total trigger efficiency, i.e. L1×HLT.

Samples	L1 e$*\tau$ (%)	L1 $\mu*\tau$ (%)	HLT e$*\tau$ (%)	HLT $\mu*\tau$ (%)	Total (%)
$\phi \to \tau\tau$ bb	44.3 ± 0.7	54.8 ± 0.7	7.0 ± 0.3	5.9 ± 0.3	6.0 ± 0.2
tt_{had}	28.7 ± 0.2	32.1 ± 0.2	0.35 ± 0.02	0.49 ± 0.02	0.57 ± 0.02
tt_{tau}	22.6 ± 0.2	42.5 ± 0.2	1.4 ± 0.2	2.8 ± 0.2	3.1 ± 0.2
Zbb	5.6 ± 0.2	10.7 ± 0.2	2.0 ± 0.2	3.1 ± 0.2	1.4 ± 0.2
Z+jets	2.6 ± 0.2	4.6 ± 0.2	0.55 ± 0.02	0.74 ± 0.02	0.35 ± 0.02
W+jets	22.8 ± 0.2	23.1 ± 0.2	0.22 ± 0.02	0.31 ± 0.02	0.039 ± 0.002

invariant mass is estimated from the reconstructed momenta of the two τ's. Finally the b jets from the other Higgs boson decay are reconstructed.

5.2.1 $\tau\tau$ invariant mass

In order to reconstruct the $\tau\tau$ invariant mass, the neutrino momentum has to be reconstruted. The vector sum of the transverse momenta of the two neutrinos is measured as the total missing transverse momentum in the event. To separate the contribution from the two neutrinos the *collinear approximation* can be used: if the τ momentum is much larger than m_τ, the neutrino momentum and the momentum of the visible τ decay products can be assumed to be collinear. The total missing momentum projected on the τ-jet (or lepton) direction in the transverse plane thus gives the transverse momentum of the corresponding neutrino, p_T^ν. The $\tau\tau$ invariant mass ($M_{\tau\tau}$) distribution is shown in Fig. 16(a,b) for both the background and the signal. The tail at large invariant mass values in the signal distribution is mainly due to the events with two τ's in a back-to-back configurations in the transverse plane. In fact, the mass resolution is proportional to the missing E_T resolution and to 1/sin($\Delta\phi_{jj}$), where $\Delta\phi_{jj}$ is the azimuthal angle between the two jets [27]. The fit to the Gaussian part of the signal distribution, shown in Fig. 16, gives a Higgs boson mass value about 10% higher than simulated due to the absence of missing E_T corrections.

5.2.2 Selection of jets and di-jet invariant mass

At least two jets are required with a transverse energy greater than 30 GeV and $|\eta|$ <2.1. At least one jet is required to be tagged as a b jet. The b tagging efficiency is 0.65 for signal events. If more than one jet is tagged as b jet, then the most energetic two b jets are considered. If only one jet is tagged then the most energetic jet (not tagged as τ or b jet) is taken. The di-jet invariant mass when at least one jet is tagged as b jet (M_{bj}) is shown in Figure 16(c,d) for both the background and the signal. Incorrect b tagging and pairing degrades the mass resolution from 18 to 30 GeV/c^2. Figure 17 shows the di-jet invariant mass for signal events with the correct jet–b–quark association for both jets.

5.2.3 Other selections

Finally, to further suppress the background, the E_T of the most energetic jet is required to be larger than 55 GeV and the transverse invariant mass of the lepton and the missing transverse momentum ($M_T^{\ell\nu}$) to be below 35 GeV/c^2. The corresponding distributions are shown in Fig. 18. The cut on $M_T^{\ell\nu}$ efficiently suppresses the $t\bar{t}$ and W+jets backgrounds, while the cut on the maximal jet E_T suppresses the Z+jets background.
The helicity angle distributions, i.e. the distributions of the angle between the jets and the Higgs boson flight direction in the rest frame of the Higgs boson and the distribution of the angle between the Higgs boson and the radion direction in the rest frame of the radion, have been also considered. For scalar

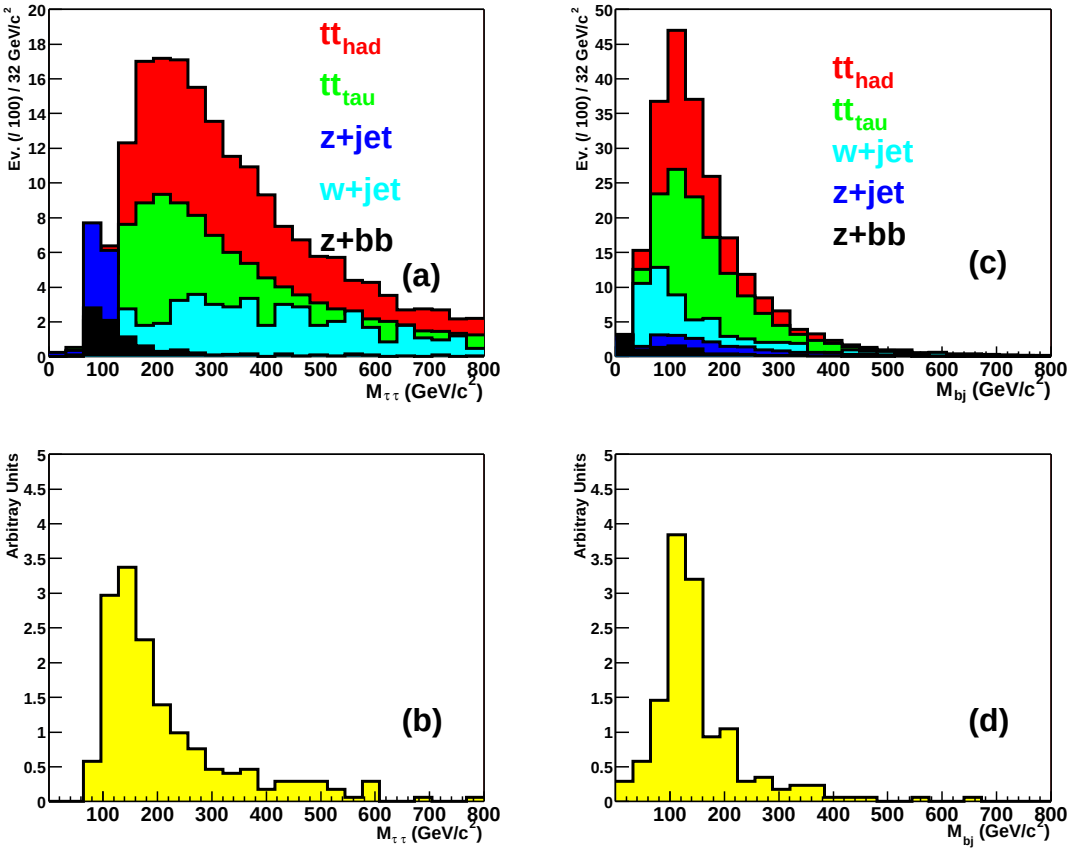

Figure 16: The distributions of $M_{\tau\tau}$ and M_{bj} for the background (a,c) and the signal (b,d). The tt_{had} is the sample with one W decaying into electron or muon and the other decaying hadronically. The tt_{tau} is the sample with one W decaying into τ and the other decaying hadronically (Table 2).

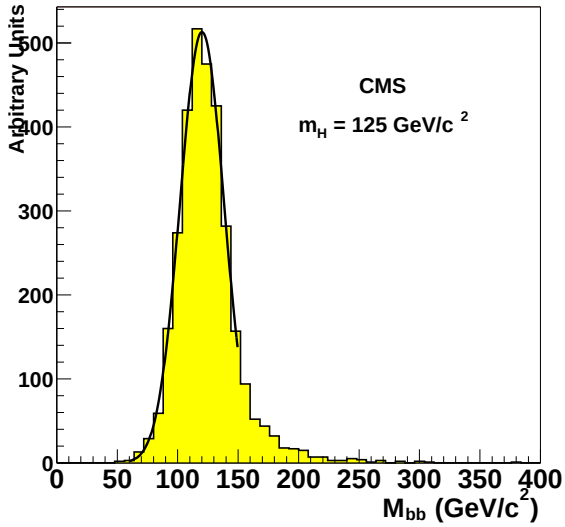

Figure 17: Invariant mass calculated from true b-jets produced in the Higgs boson decay, for signal events.

particles the distributions of the cosine of these angles are expected to be flat. However they have been found not to be discriminant with respect to the background selection, mainly due to the fact that the

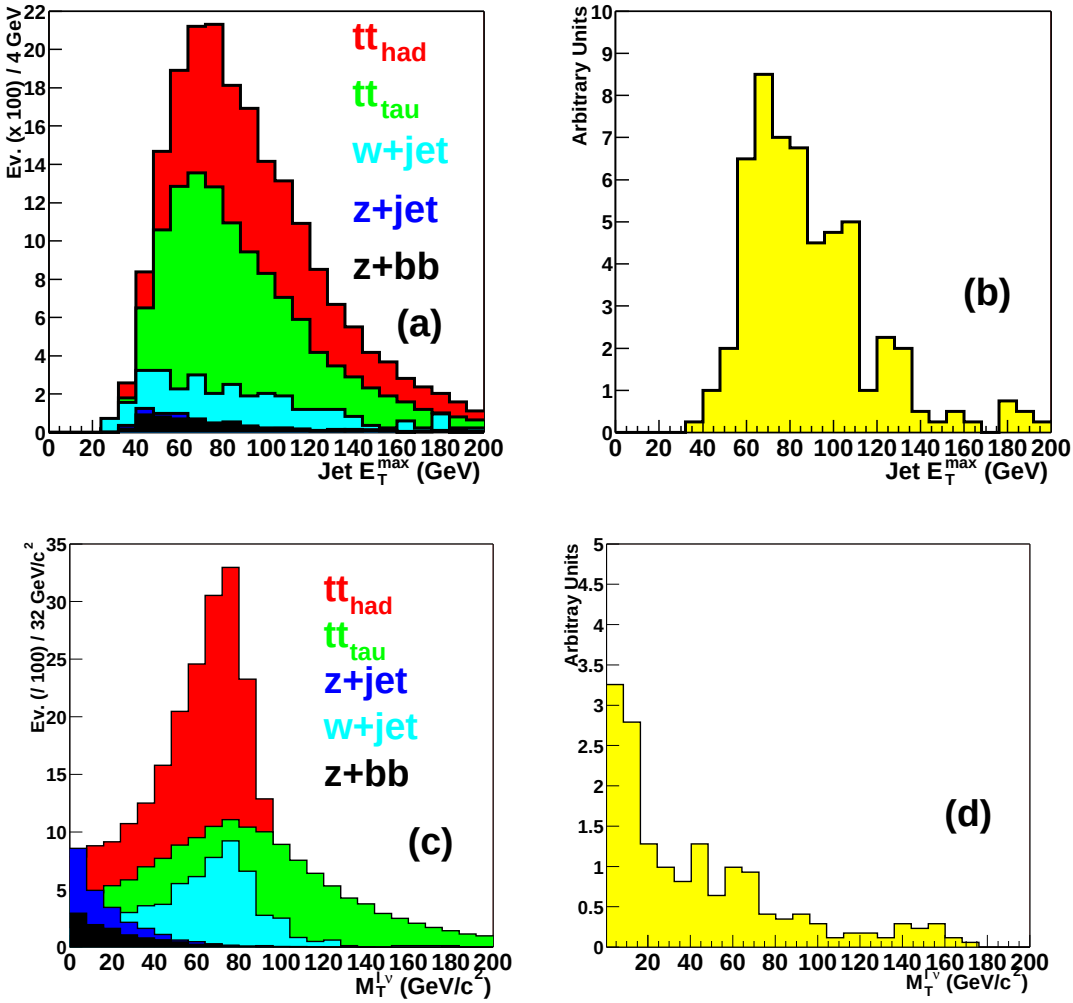

Figure 18: Distributions of the jet maximal $\mathrm{E_T}$ (a,b). Transverse invariant mass of the lepton and the missing momentum (c,d). The left top and bottom plots refers to the background samples, the right top and bottom plots refers to the signal sample.

Higgs bosons are not relativistic.

5.3 Radion mass reconstruction

As discussed in section 4.6.5, the Higgs boson mass should be known from the analysis of the $\gamma\gamma\mathrm{b\bar{b}}$ analysis. In the following the assumption is made that the Higgs boson mass is known with a precision of at about 1%. Given the jet invariant mass resolution inferred from the simulation, the following cuts were applied to select signal events:

- b-tagged jets reconstructed invariant mass: $100 < M_{\mathrm{bj}} < 150$ GeV/c^2;
- τ jets reconstructed invariant mass: $100 < M_{\tau\tau} < 160$ GeV/c^2.

The energy of the reconstructed jets can be rescaled using a kinematic fit that constrains the reconstructed invariant masses be equal to the known Higgs boson mass. In this way a much better resolution on the radion mass can be achieved.

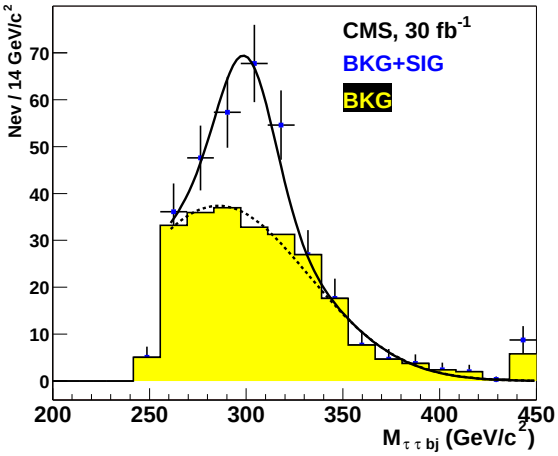

Figure 19: Reconstructed radion mass, for signal plus background.

5.3.1 Signal extraction

Figure 19 shows the fitted radion mass ($M_{\tau\tau\mathrm{bj}}$) for signal plus background for the maximal signal cross section. The background shape can be extracted with good precision from the data as shown in the next section. For a radion mass of 300 GeV/c^2 a mass resolution of about 5% is expected. The signal–plus–background fit is performed using two Gaussian. The signal Gaussian has a mean of 300 GeV/c^2 and a width of 15 GeV/c^2. The background function is centred around 285 GeV/c^2 with a width of about 45 GeV/c^2. In the fit only the relative weights have been left free in order to extract the number of signal and background events from the fit.. The number of the background events can be extracted with a precision better than 10%. A further selection on this reconstructed mass is then applied: $290 < M_{\tau\tau\mathrm{bj}} < 330$ GeV/c^2. Table 9 shows the numbers of signal and background events expected after all the selections. The final signal efficiency is about 0.27%, while the background efficiency is less than 3×10^{-5}.

Table 9: Number of expected events for signal and backgrounds, after all the selections.

Samples	Number of events expected
$\phi \to \tau\tau$ bb	79
$\mathrm{tt_{had}}$	40
$\mathrm{tt_{tau}}$	24
Zbb	13
Z+jets	7
W+jets	0

The total number of background events after all the selections, with an integrated luminosity of 30 fb^{-1}, is 84. The largest background contribution comes from the $\mathrm{t\bar{t}}$ sample (64 events), while the W+jets background is negligible. The contribution of the top pair sample with both W's decaying into τ (which has not been simulated) has been estimated to amount of an additional 8 events, so that the total number of background events is ~ 92.
The number of signal events depends on the choice of the ξ and Λ_ϕ parameters. For the largest cross section of 0.96 pb, ($\xi = -0.35$ and Λ_ϕ=1 TeV) about 79 signal events are expected, yielding a significance greater than 8. Figure 20a shows 5σ discovery contour in the (ξ, Λ_ϕ). Inside this contour the production cross section of the $\gamma\gamma\mathrm{b\bar{b}}$ final state is not smaller than the 65% of the largest possible value for the $\gamma\gamma\mathrm{b\bar{b}}$ mode. With this cross section the Higgs boson mass is known from the observed peak in the di-photon

mass distribution of the $\gamma\gamma$bj events and the accuracy of the Higgs boson mass measurement is better than 1%. The effect of the uncertainties on the NLO cross section is also shown in Fig. 20a. The area with the maximum extension is obtained by assuming the minimum NLO cross section while the other assuming the maximum one (Table 3). Figure 20b shows the excluded region at the 95% confidence level in the (ξ, Λ_ϕ) plane. No uncertainties on the NLO cross section have been taken into account in this figure. More details on the extraction of the 95% confidence level region can be found in [28].

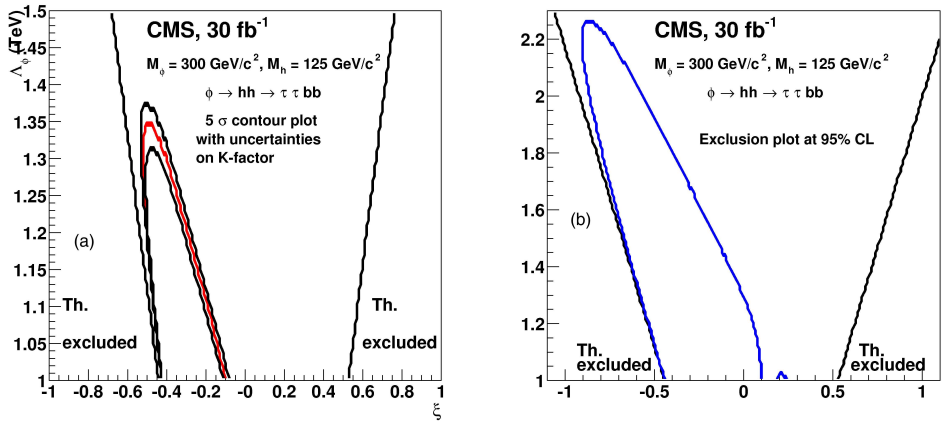

Figure 20: (a) The 5σ discovery contour considering the maximum and minimum NLO cross sections (Table 3). Only statistical uncertainties have been considered. (b) The 95% CL exclusion region. No NLO uncertainties have been considered in the figure.

5.3.2 Evaluation of background from the data and effect of systematics

The extraction of the background shape for the radion invariant mass ($M_{\tau\tau\mathrm{bj}}$) is performed by studying the background distributions after the trigger and off-line selections in a signal free region.
The Z decays into electrons and muons can be used to have a control sample for the Z+jets and Z$\mathrm{b\bar{b}}$ backgrounds. In this case the value of the τ-tagging efficiency and the efficiencies of invariant mass selections ($M_{\tau\tau}$ and M_{bj}) must be known from the simulation. They can be measured with pure Z events, by evaluating the ratio between the number of events in which the Z decays into τ leptons (with one τ jet in the final state) and the number of events in which the Z decays into electron and muons. Detailed studies have never been done, but statistics would allow a measurement with an accuracy of the order of 5%.
For the top and W samples, events in a signal free region are selected by requiring the transverse invariant mass distribution of the lepton and the missing energy ($\mathrm{M_T^{\ell\nu}}$) to be larger than 30 GeV/c^2. In this region, the signal contribution is below 1.5% (with the maximum cross section). The contribution from the Z+jets events is negligible (Figure 21). It is possible, with this background control sample, to extract the shape of the $M_{\tau\tau\mathrm{bj}}$ distribution after the b and τ jets tagging. A Gaussian fit to the distribution of the top and W+jets samples gives a mean value of about 292 GeV/c^2, while the fit to the total background has a mean value of 285 GeV/c^2. The width of the Gaussian is about 46 GeV/c^2 in both cases (total background and top and W+jets samples only). The shift of few GeV/c^2 is related to the contribution of the Z+jets background. Detailed studies are needed to understand better the precision with which these backgrounds will be known at LHC and to study the possible correlations between the variables used in the selection. A more sophisticated fitting function could lead to precision below 10%. An uncertanty of 5 to 10% has been considered in this work.
To include systematic uncertainties, the following formula was used

$$\mathrm{significance} = \mathrm{N_{sig}}/\sqrt{\mathrm{N_{bkg}} + (\delta_{\mathrm{sys}} \times \mathrm{N_{bkg}})^2},$$

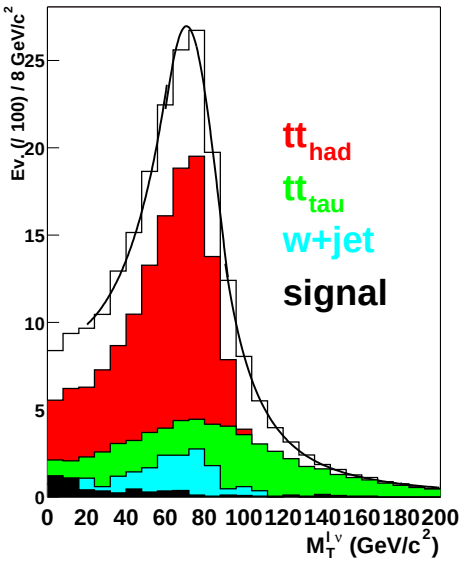

Figure 21: Transverse invariant mass of lepton and missing energy distribution for the top and W+jet samples and the signal. The black line is the fit at the sum of the background samples (without the signal).

where δ_{sys} is the systematic uncertainty on the background. Figure 22 shows the discovery plot for a systematic uncertainty of 5% (a) and for 10% (b). With a systematic uncertainty of 10% Λ_ϕ values below 2 TeV can be excluded, instead of 2.3 TeV in the absence of systematic uncertainties.

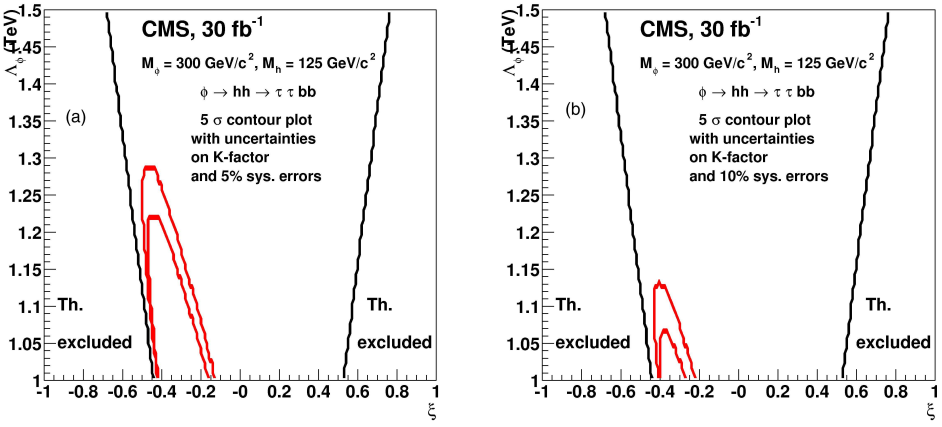

Figure 22: 5σ discovery contour considering the maximum and minimum NLO cross section and systematic uncertainties of 5% (a) and 10% (b) on background.

6 Analysis of the $\mathrm{b\bar{b}b\bar{b}}$ final state

The four b-jet final state yields the highest rate for the signal. The maximal cross section times branching ratio at Λ_ϕ= 1 TeV is 10.3 pb, which results in about of 3.1×10^5 signal events for 30 fb^{-1}. The effective triggering and selection in the off-line analysis of these events is, however, a big challenge due to the huge multi-jet background rate.

6.1 Kinematical properties

In Figure 23a is shown the transverse energy of the four highest-E_T jets reconstructed at the generator level with the cone algorithm using the cone size of 0.4. In Figure 23b the pseudorapidity distribution of these jets for the signal and the four b-jet background from QCD multi-jet production are shown. The signal events were processed with both the full and the fast detector simulation. The number of the

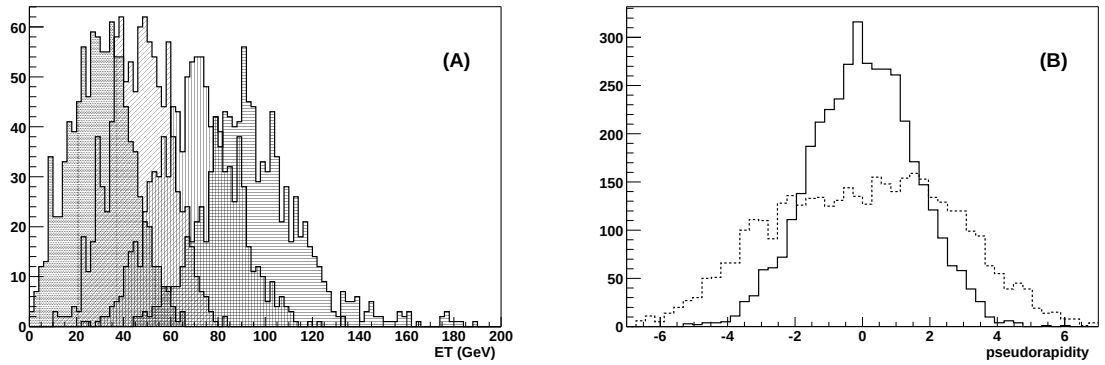

Figure 23: (a) Transverse momentum distributions for the four highest-E_T jets ordered in increasing E_T. (b) Pseudorapidity distribution of the four highest-E_T jets for the signal (full histogramm) and QCD with four b jets in the final state (dashed histogramm).

reconstructed jet with $E_T > 30$ GeV and the number of the jets tagged as b jets are shown in Figure 24 for the fast simulated signal events.

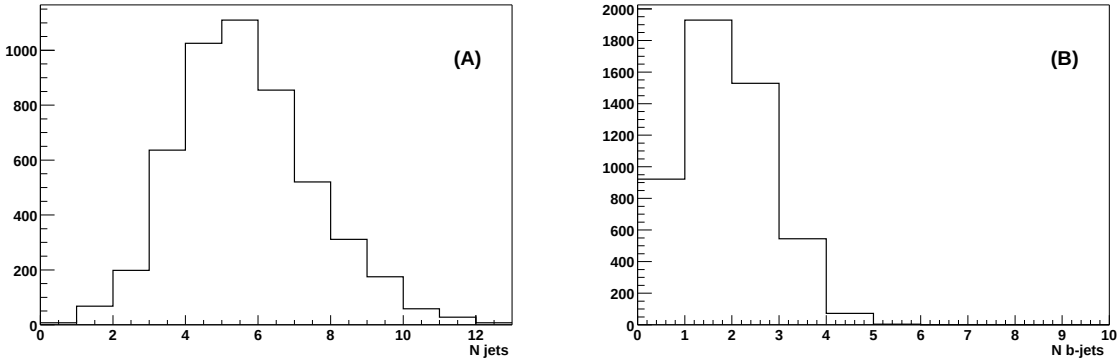

Figure 24: Mean number of reconstructed jets (a) and b-tagged jets (b) for the fast simulated signal events. The transverse energy of jets is required to be larger than 30 GeV

6.2 The Level-1 trigger and HLT selection

If at least four jets are required with $E_T > 50$ GeV, the selection efficiency is $\sim$10% for the signal and $\sim$10% for QCD multi-jet background ($\hat{p}_T >$100 GeV/c).

To reach a more efficient signal/background separation, the trigger strategy is optimized as follows:

- At Level-1, the multi-jet trigger with the thresholds taken from Table 15-13 of the CMS DAQ TDR [21] is applied.
- At the High-Level trigger, at least four jets with $E_T > 30$ GeV are required with y below 0.8 and two of them have to be tagged as b jets.

Table 10 shows the efficiency of the Level-1 trigger and the total selection (Level-1 + High-Level trigger + offline) for the signal and the backgrounds. For the cases in which no background events are left

after the selections, 95% CL upper limits are given. The QCD multi-jet event rate after the Level-1 and High-Level trigger selection is about 5 Hz.

6.3 Offline analysis

All possible di-jet invariant masses were calculated from the four highest-E_T jets selected at High-Level trigger. The two jet pairs that minimize the value of $\mid m_{i,j}\text{-}m_{k,l} \mid$ were chosen; the reconstructed Higgs boson mass m_h^{reco} was calculated as the mean value of the two di-jet masses. The same jets were used to reconstruct the radion mass m_ϕ^{reco}. The distributions of m_h^{reco} and m_ϕ^{reco} obtained with the fast detector simulation for the signal events are shown in Figure 25(a,b). The resolution of m_h^{reco} is 39 GeV/c^2, a factor two larger than the resolution obtained for the events with the correct jet-b quark association for all four jets (Figure 25c). Figure 25d shows the m_ϕ^{reco} distribution obtained with the full detector simulation. A 1.5σ mass window around m_h and m_ϕ were used to select the signal events.

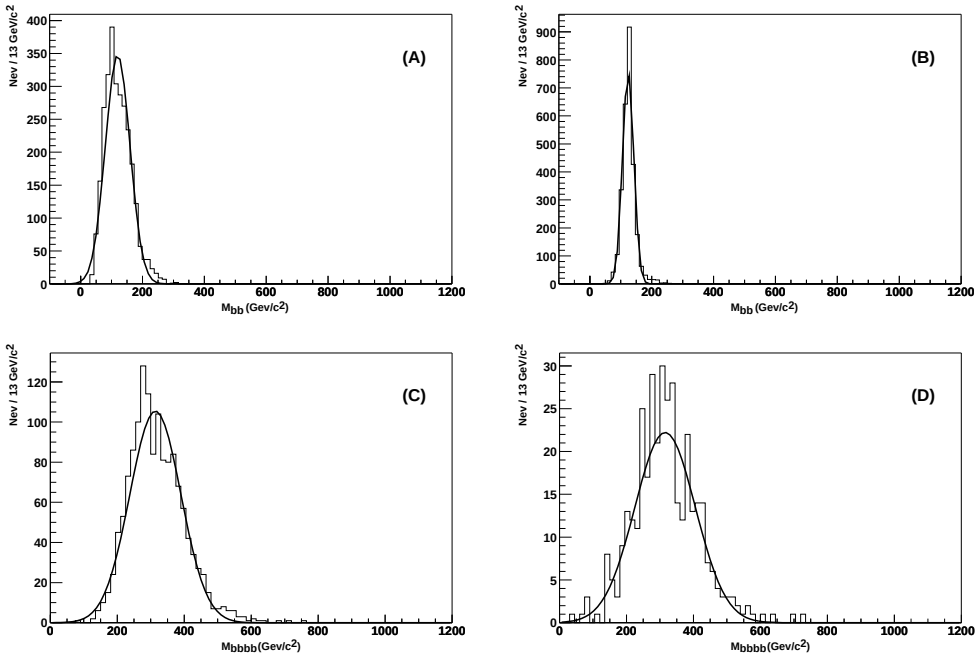

Figure 25: (a): m_h^{reco} distribution; (c) : m_h^{reco} distribution with the correct jet-b quark associations; (b) and (d): m_ϕ^{reco} distributions obtained with the fast and the full detector simulations.

Efficiencies for the signal, background and the expected number of events with 30 fb^{-1} after all selections are given in Table 10.

Table 10: Trigger and off-line selection efficiencies for the signal and the background; the number of events expected with 30 fb^{-1} after all selections.

	$\epsilon_{trigger}$	$\epsilon_{L1+HLT+offline}$	N events with 30 fb^{-1}
signal	0.038	0.031	$9.57{\cdot}10^3$
QCD $\hat{p}_T$ (30-50) GeV/c^2	$< 1.1{\cdot}10^{-7}$	$< 1{\cdot}10^{-7}$	$< 5.7{\cdot}10^5$
QCD $\hat{p}_T$ (50-80) GeV/c^2	$< 5{\cdot}10^{-7}$	$< 5{\cdot}10^{-7}$	$< 3.8{\cdot}10^5$
QCD $\hat{p}_T$ (80-120) GeV/c^2	$1{\cdot}10^{-5}$	$7{\cdot}10^{-6}$	$7.5{\cdot}10^5$
QCD $\hat{p}_T$ (120-170) GeV/c^2	$1{\cdot}10^{-4}$	$6.6{\cdot}10^{-5}$	$1.1{\cdot}10^6$
$t\bar{t}$	0.015	0.010	$1.84{\cdot}10^5$
$Zb\bar{b} \rightarrow 4b$	0.0022	$8{\cdot}10^{-4}$	$1.2{\cdot}10^3$

6.4 Four b-jet background from QCD multi-jet production

From fast simulation estimation it is expected to find four b quarks in the final state in less than 10^6 events from QCD multi-jet events with $\hat{p}_T < 100$ GeV/c and about $1.6 \cdot 10^6$ with $\hat{p}_T > 100$ GeV/c with 30 fb^{-1}. In the case of $\hat{p}_T > 100$ GeV/c, selection (at generator level) of the final states containing four bottom quarks yields a contribution of about $1.2 \cdot 10^6$ (with a corresponding cross section of $2 \cdot 10^{-6}$ mb). The difference of about 25% can be reasonably due to the fast simulation mistagging effect on c and light quarks: 10% and 1.2% respectively [30]. Figure 26 shows the flavour content against different cuts on the b-tag variable used in CMSJET [18].

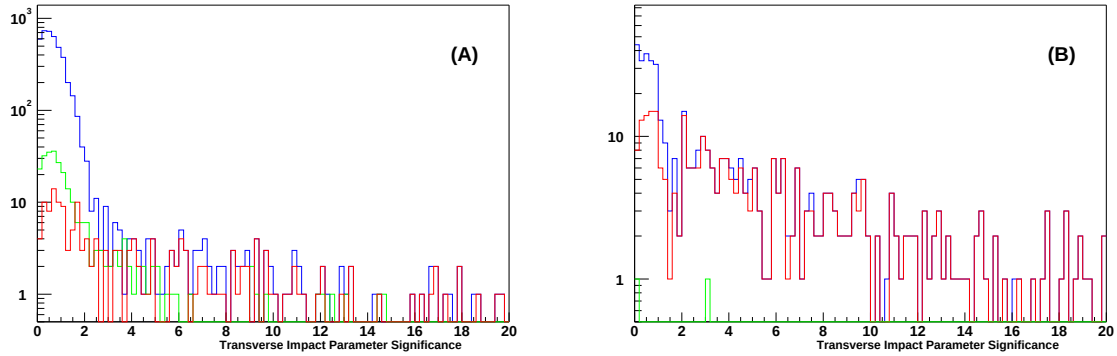

Figure 26: Flavour content for the QCD multi-jet events (a) and for QCD multi-jet events events containing four b quarks (b) with $\hat{p}_T$ >100 GeV/c: solid line - jets from light quarks, dotted line - b-jets, light dotted line - c-jets.

6.5 Discovery potential

At the maximal signal cross section times branching ratio point the statistical significance $S/\sqrt{B}$ is 5.5 with 30 fb $^{-1}$. Figure 27 shows the m_h^{reco} and m_ϕ^{reco} mass distributions for the signal at the maximal rate point and for the background with 30 fb^{-1} after all selections.

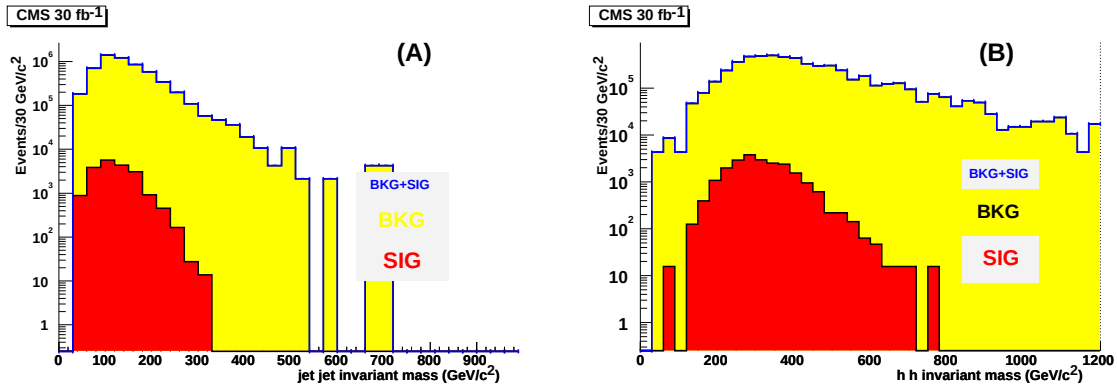

Figure 27: The m_h^{reco} (a) and the m_ϕ^{reco} (b) mass distributions for the signal and the background with 30 fb^{-1} at the maximal signal cross-section times branching ratio point.

6.6 Systematic uncertainties

The main sources of systematic uncertainies due to the detector reconstruction and selections are the jet energy scale uncertainty expected to be about of 1% [21] and the uncertainty of the b-tagging efficiency expected to be an order of $\sim$ 1%. The theoretical uncertainty on the multi-jet background production cross section is at least 10% [31]. The luminosity uncertainty is of the order of 3-5 % [29]. With the huge

number of the background events the systematic uncertainty is bigger than the number of signal events expected even for the maximal cross section times branching ratio point. A possible way to improve the situation is to normalize the background directly from the data in a signal free region of the four-jet invariant mass (assuming that the radion and the Higgs boson masses are known from the other channels) and predict the number of the background events in the region of the signal. The systematic uncertainty in this way is dominated by the theoretical error of the knowledge of the background shape. In order to still have the 5σ discovery at the maximal cross section times branching ratio point the uncertainty of the extrapolation should be less than 0.1%. This requirement makes four b-quark final state mostly hopeless.

7 CONCLUSION

The CMS discovery potential has been estimated for the radion into two Higgs decay mode ($\phi \rightarrow \mathrm{hh}$) in the $\gamma\gamma\mathrm{b\bar{b}}$, $\tau^+\tau^-\mathrm{b\bar{b}}$ and $\mathrm{b\bar{b}b\bar{b}}$ final states. The point of m_ϕ=300 GeV/c^2 and $\mathrm{m_h}$=125 GeV/c^2 has been studied and the observability in the (ξ, Λ_ϕ) plane has been evaluated. It has been found that the $\gamma\gamma\mathrm{b\bar{b}}$ topology provides the best discovery potential. The $\tau\tau\mathrm{b\bar{b}}$ topology can explore about the half of the region in the (ξ, Λ_ϕ) plane where $\gamma\gamma\mathrm{b\bar{b}}$ mode is discovered. The discovery with the $\mathrm{b\bar{b}b\bar{b}}$ mode is mostly hopeless.

ACKNOWLEDGEMENTS

A.N. would like to thank M. Dubinin for CompHEP generation of $\gamma\gamma\mathrm{jj}$ events and F.Maltoni for explanations about the MadGraph generator. D.D. would like to thank M. Battaglia, S. De Curtis, A. De Roeck, B. Grzadkowski, J. Gunion and M. Toharia for their collaboration on the Higgs-radion phenomenology.

Authors are greatful to the referees J. Varela and F. Palla and the members of the CMS PRS Editorial Board P. Janot and N. Marinelli for very useful discussions and corrections.

References

[1] Randall, L. and Sundrum, R., Phys. Rev. Lett. **83** (1999), 3370.

[2] Randall, L. and Sundrum, R., Phys. Rev. Lett. **83** (1999), 4690.

[3] M. Carena and H.E.Haber, Higgs Boson Theory and Phenomenology, hep-ph/0208209, Published in Prog. Part. Nucl. Phys. 50 (2003) 63-152.

[4] Giudice, G. F., Rattazzi, R., Wells, J. D. Nucl. Phys. **B 595** (2001), 250.

[5] Chaichian, M., Datta, A., Huitu, K, Yu, Z. h., Phys.Lett. **B 524** (2002), 161.

[6] Hewett, J. L. and Rizzo, T. G., J. High Energy Phys. **08** (2003) 028

[7] Dominici, D., Grzadkowski, B., Gunion, J. F., Toharia. M., The scalar sector of the Randall-Sundrum model, hep-ph/0206192, Published in Nucl. Phys., **B 671** (2003) 243-292.

[8] Battaglia, M., Curtis, S. De, Roeck, A. De, Dominici, D., Gunion J. F., Phys. Lett. **B 568** (2003) 92-102.

[9] Azuelos, G., Cavalli, D., Przysiezniak, H., Vacavant, L., Search for the radion using the ATLAS detector, SN-ATLAS-2002-019.

[10] T. Sjostrand, *PYTHIA 6.2 Physics and Manual*, hep-ph/0108264.

[11] M.Spira, HIGLU and HDECAY : Programs for Higgs Boson Production at the LHC and Higgs Boson Decay Widths, hep-ph/9610350; A.Djouadi, J.Kalinowski, M.Spira, HDECAY : a Program for Higgs Boson Decays in the Standard Model and its Supersymmetric Extension, hep-ph/9704448, Published in Comput. Phys. Commun. 108 (1998) 56; M. Spira, http://people.web.psi.ch/spira/proglist.html

[12] A. Pukhov et. al., CompHEP : a package for evaluation of Feynman diagrams and integration over multi-particle phase space, hep-ph/9908288;

[13] F. Maltoni and T. Stelzer, JHEP **0302**, 027 (2003); T. Stelzer and W. F. Long, Comput. Phys. Commun.**81** (1994) 357.

[14] Z. Kunszt, private communication

[15] S. Shevchenko, private communication

[16] U. Baur, T. Plehn, D. Rainwater. CERN-TH/2003-186.

[17] J. Campbell, *at al.*, Phys. Rev. **D 68** (2003) 094021; D. Chakraborty, *at al.*, Review of Top Quark Physics, hep-ph/0303092.

[18] S. Abdullin *et al.*, CMS TN/94-180, CMSJET.

[19] G. Segneri and F. Palla, Lifetime Based b-tagging with CMS, CMS NOTE 2002/046.

[20] CERN/LHCC 97-33, CMS TDR 4 (1997).

[21] CMS Collaboration, CERN/LHCC/2002-26, CMS TDR 6.2 15 (2002).

[22] V. Litvin, H. Newman, S. Shevchenko, N. Wishiewski, private communication.

[23] V. Litvin, H. Newman, S. Shevchenko, private communication.

[24] S. Rutherford, Study of the Effects of Data Reduction Algorithms on Physics Reconsruction in the CMS ECAL, CMS NOTE-2003/001.

[25] F. Maltoni, private communication

[26] S. Abdullin et al., Summary of the CMS Potential for the Higgs Boson Discovery, CMS Note 2003/033, Submitted as Scientific note in EPJCdirect.

[27] A. Nikitenko, S. Kunori and R. Kinnunen, Missing Transverse Energy Measurement with Jet Energy Corrections, CMS Note 2001/040.

[28] J. Conway, FERMILAB-Conf-00/048-E CDF (2000).

[29] A. De Roeck private communication.

[30] V. Drollinger, V. Karimaki, S. Lehti, N. Stepanov and A. Khanov, private communication.

[31] Ppoceedings of the Workshop on Standard Model Physics (and more) at the LHC, CERN 2000-04 (2000).